

Simplified Reactive Power Control for Single-Phase Grid-Connected Photovoltaic Inverters

Chia-Hsi Chang, *Student Member, IEEE*, Yu-Hui Lin, Yaow-Ming Chen, *Senior Member, IEEE*, and Yung-Ruei Chang, *Member, IEEE*

Abstract—The objective of this paper is to propose a simplified reactive power control (SRPC) strategy for single-phase grid-tied photovoltaic (PV) inverters. With the proposed SRPC strategy, a cost-effective microcontroller can be adopted to achieve an effectively reactive power control. Moreover, the current-mode asynchronous sigma-delta modulation (CASDM) is adopted to enhance the current control's dynamic response and reduce both the current harmonic distortion and electromagnetic interference. In this paper, the operational principle of the proposed SRPC is introduced. Then, the small signal analysis for the PV inverter with the CASDM is presented. Finally, a 1-kVA single-phase PV inverter was built to verify the performance of the proposed control strategy.

Index Terms—Asynchronous sigma-delta modulation (ASDM), current-mode control, photovoltaic (PV) inverter, reactive power control (RPC), single-phase.

I. INTRODUCTION

BECAUSE of its quietness and cleanness, the photovoltaic (PV) power generation system has become the most promising renewable energy source for residential applications [1], [2]. Since the best way to utilize the PV power is to inject it into the ac mains without using energy storage facilities, the grid-connected PV inverter is always necessary for the PV power system [3], [4]. Moreover, the PV inverter is a potential candidate to provide reactive power for the utility grid to improve its power quality. As a result, the PV inverter with the reactive power supply has a very important role in the PV power system nowadays [5], [6].

In order to accurately control the reactive output power, the current reference generation (CRG), which can generate the proper current reference with demanded power components, should be established in advance. In different literature, many reactive power control (RPC) strategies for the single-phase inverter have been proposed [2], [7]–[14]. Among them, the direct-quadrature (d-q) transformation [7], [8] and the instantaneous reactive power theory (the p-q theory) [9]–[11] are the most addressed control schemes to generate two orthogonal current references. Furthermore, some modified methods were

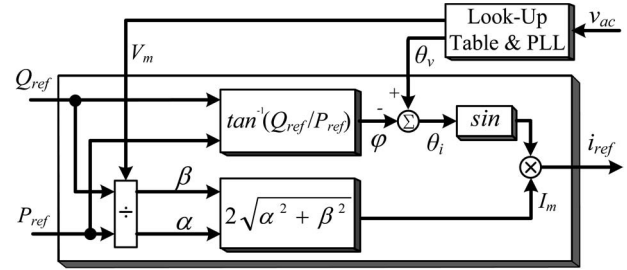


Fig. 1. Block diagram of the CRG using scalar control method.

presented to improve the controlled performance. The authors in [12] adopted a sinusoidal signal integrator along with the p-q theory to reduce the controlled sensitivity to the grid voltage distortion. While the authors in [13] used the discrete Fourier transform phase lock loop (PLL) method to achieve more precise RPC. Although those methods are effective, the powerful computer platform, dSPACE, is needed to deal with those sophisticated functions, such as advanced signal filters, coordinate transforms, or Fourier transforms.

Alternatively, the scalar control method has been proposed to simplify the CRG [2], [14]. The block diagram of CRG using the scalar control method is shown in Fig. 1. The amplitude and the phase angle of the current reference are easily determined by the measured parameters, which include the grid voltage's amplitude and phase angle, and several calculations. However, many complicated functions are still required, particularly the arc tangent function, so the reduction of computational burden is limited. On the other hand, the CRG only generates the demanded current reference. There is no ac current feedback, so the information of both the active and the reactive power is unknown. Once the amplitude or the phase angle of the output current is not equal to its reference, it will lead to incorrect active/reactive power generation.

In order to further reduce the computational burden of the controller as well as to reduce the cost of the hardware circuit, a simplified power calculation, where the active power and the reactive power can be easily calculated by two sampled current values within one ac mains cycle, is proposed in this paper. The simplified power calculation along with a smooth power adjustment forms a simplified RPC (SRPC) strategy. With the SRPC, the CRG can be simplified significantly, and the cost-effective microcontroller can be used to achieve the RPC. Moreover, in order to reduce the controlled sensitivity to the grid current distortion, the current-mode asynchronous sigma-delta modulation (ASDM) (CASDM), which has the merit of fast dynamic response, low current harmonic distortion, and low

Manuscript received January 20, 2013; revised April 10, 2013 and June 5, 2013; accepted June 9, 2013. Date of publication June 28, 2013; date of current version October 18, 2013.

C.-H. Chang, Y.-H. Lin, and Y.-M. Chen are with the Electric Energy Processing Laboratory (EEPro), Department of Electrical Engineering, National Taiwan University, Taipei 106, Taiwan (e-mail: f97921017@ntu.edu.tw; f98921023@ntu.edu.tw; ymchen@cc.ee.ntu.edu.tw).

Y.-R. Chang is with the Institute of Nuclear Energy Research, Atomic Energy Council, Taoyuan 32546, Taiwan (e-mail: raymond@iner.gov.tw).

Color versions of one or more of the figures in this paper are available online at <http://ieeexplore.ieee.org>.

Digital Object Identifier 10.1109/TIE.2013.2271600

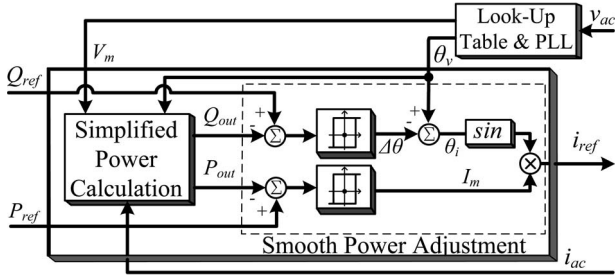


Fig. 2. CRG with the proposed SRPC method.

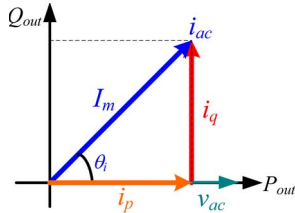


Fig. 3. Phasor diagram of the ac output current.

electromagnetic interference, is adopted for the PV inverter's output current control strategy [15]–[17].

This paper is organized as follows. The operational principle and mathematic derivation of the proposed SRPC method are described in Section II. Then, the small signal analysis for the PV inverter with the CASDM is presented in Section III. Finally, a 1-kVA single-phase PV inverter was built to verify the performance of the proposed RPC strategy.

II. PROPOSED SRPC METHOD

In order to reduce the computational burden of the processor as well as to improve the controlled accuracy, the SRPC method, as shown in Fig. 2, is proposed. The proposed SRPC method, which consists of a simplified power calculation and a smooth power adjustment, can simplify the CRG of the grid-connected PV inverter.

A. Simplified Power Calculation

The simplified power calculation, in which the active power and the reactive power can be easily calculated by two sampled current values within one ac mains cycle, is proposed in this paper. First, the grid voltage is assumed to be a purely sinusoidal waveform, so the inverter's output power is determined directly by its injected sinusoidal current.

The typical phasor diagram of the inverter's output current i_{ac} is shown in Fig. 3. The active power is produced by the current component i_p which is in phase with grid voltage v_{ac} , and the reactive power is controlled by the current i_q which is 90° out of phase with the voltage v_{ac} . The amplitudes of the currents i_p and i_q can be expressed

$$i_p = I_m \cos \theta_i \quad (1)$$

$$i_q = I_m \sin \theta_i \quad (2)$$

where I_m and θ_i are the amplitude and phase angle of the current i_{ac} , respectively. By controlling the I_m and the θ_i of the current i_{ac} , the active and reactive power control can be achieved. The principle of the proposed simplified power calculation method can be explained by using the typical grid

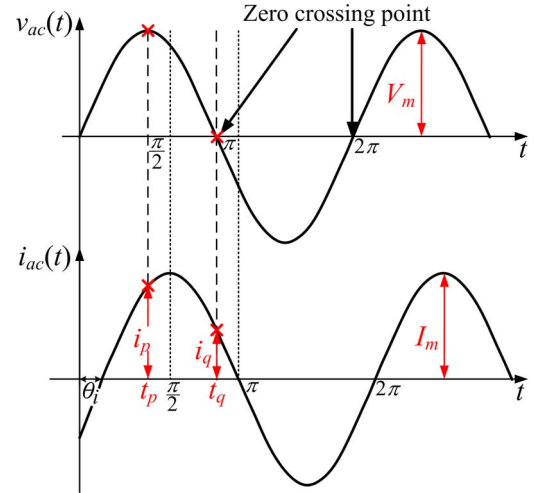


Fig. 4. Typical voltage and current waveforms of the ac mains.

voltage and current waveforms shown in Fig. 4. The voltage and current waveforms can be expressed

$$v_{ac}(t) = V_m \sin \omega t \quad (3)$$

$$i_{ac}(t) = I_m \sin(\omega t - \theta_i) \quad (4)$$

where ω is the line frequency of the ac mains in radians per second.

At time t_p , the amplitude of the injected ac current is expressed as

$$i_{ac}(t_p) = I_m \sin(\pi/2 - \theta_i) = I_m \cos \theta_i. \quad (5)$$

It should be mentioned that the current i_p can be measured by delaying a quarter of the ac line period when the zero crossing point of the ac mains voltage v_{ac} is detected. Equation (5) reveals that the sampled quantity at time t_p is equal to the amplitude of the active current component i_p .

Thus, the active output power of the inverter can be determined as

$$P_{out} = \frac{1}{2} V_m I_m \cos \theta_i = \frac{1}{2} V_m i_{ac}(t_p). \quad (5.a)$$

Similarly, the amplitude of the injected ac current at time t_q is

$$i_{ac}(t_q) = I_m \sin(\pi - \theta_i) = I_m \sin \theta_i. \quad (6)$$

This current value can be measured when the zero crossing point of the ac mains voltage v_{ac} is detected. It is the amplitude of the reactive current component i_q , and the reactive output power of the inverter becomes

$$Q_{out} = \frac{1}{2} V_m I_m \sin \theta_i = \frac{1}{2} V_m i_{ac}(t_q). \quad (6.a)$$

From the aforementioned equations, the active and the reactive power of the inverter can be easily calculated by two sampled current values within one ac line cycle. However, this method is also sensitive to either the current ripple or the current distortion. It should be mentioned that the impact of the unavoidable current ripple to the power calculation can be easily eliminated by adding a bandpass filter in the current feedback loop. Thus, it is necessary to design a good current control strategy to reduce the current distortion.

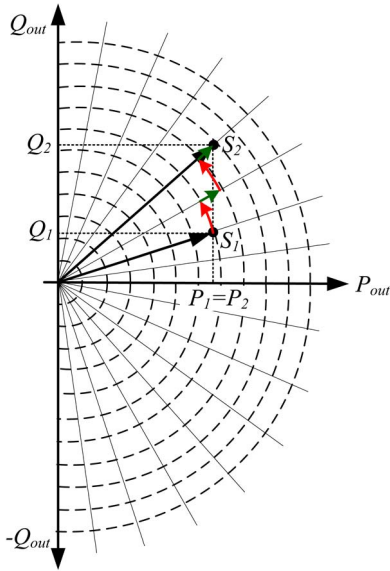


Fig. 5. Conceptual diagram of the proposed smooth power adjustment.

B. Smooth Power Adjustment

After the active power and the reactive power are obtained, a proper controller is needed to compensate the power error. In general, the proportional-integral-derivative controller has the feature of fast transient response, but the abrupt change of the ac output current may cause large current distortion which will lead to inaccurate power calculation. Therefore, a hysteresis controller, as shown in Fig. 2, is adopted to achieve smooth power adjustment.

Fig. 5 shows the conceptual diagram of the proposed smooth power adjustment. Each dashed line with the same radius represents a constant apparent power, and each solid line indicates a specific phase angle. Each intersection of the dashed line and solid line is called the operation point.

In Fig. 5, the output apparent power is changed from S_1 to S_2 with the same active power, $P_1 = P_2$, but different reactive powers, $Q_1 < Q_2$. To control the active and the reactive power of the grid-connected inverter, the power phasor should move among these operation points. By adjusting the amplitude and phase angle of the reference current cycle by cycle, the desired active and reactive output powers can be achieved smoothly. It should be mentioned that only limited operation points are shown in Fig. 5 in order to explain the control concept clearly.

Since the active output power P_{out} is regulated by changing the amplitude of the injected ac current, the measured power P_{out} is compared with the hysteresis comparator with high bound $P_{ref,H}$ and low bound $P_{ref,L}$. The positive or negative amplitude adjustment ΔI is determined by the following algorithm:

(a) The current amplitude generator

$$\begin{aligned} &\text{if } P_{out} > P_{ref,H} \text{ then } k = -1; \\ &\text{else if } P_{out} < P_{ref,L} \text{ then } k = +1; \\ &\text{else } k = 0; \\ &I_m(n+1) = I_m(n) + k \times \Delta I \end{aligned} \quad (7)$$

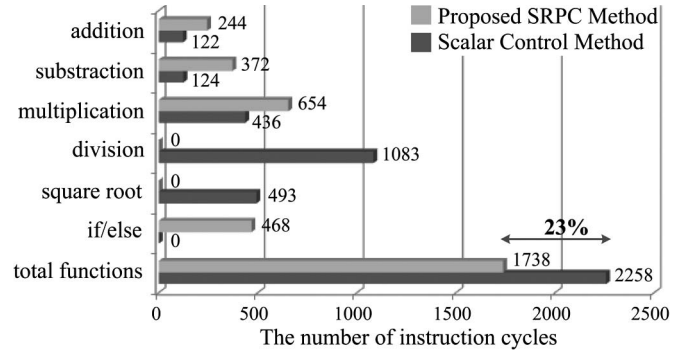


Fig. 6. Graphic comparison of computational burden.

where $I_m(n)$ and $I_m(n+1)$ are the amplitudes of the injected current reference for the n th and $(n+1)$ th ac mains cycles, respectively.

On the other hand, the reactive output power Q_{out} is regulated by adjusting the phase angle of the injected current. Similarly, the measured reactive power is compared with the hysteresis comparator with high bound $Q_{ref,H}$ and low bound $Q_{ref,L}$. The positive or negative phase shift adjustment $\Delta\theta$ is determined by the following algorithm:

(b) The current phase angle generator

$$\begin{aligned} &\text{if } Q_{out} > Q_{ref,H} \text{ then } m = -1; \\ &\text{else if } Q_{out} < Q_{ref,L} \text{ then } m = +1; \\ &\text{else } m = 0; \\ &\theta_i(n+1) = \theta_i(n) + m \times \Delta\theta \end{aligned} \quad (8)$$

where $\theta_i(n)$ and $\theta_i(n+1)$ are the phase angles of the injected current reference for the n th and $(n+1)$ th ac mains cycles, respectively.

It should be mentioned that the active power P_{out} and the reactive power Q_{out} vary with cosine and sine functions, respectively. Therefore, for θ_i close to 90° and $P_{out} \ll Q_{out}$, a change in current magnitude will cause a significant change in Q_{out} , and a change in phase angle will cause a relatively larger change in P_{out} . However, the proposed smooth power adjustment method has iterative changes in current magnitude and phase angle, so both P_{out} and Q_{out} can be adjusted correctly. Although a large value of ΔI and $\Delta\theta$ may lead to relatively fast dynamic response, the large active/reactive power fluctuation under steady state will happen. On the contrary, the power transition will take a long time if the ΔI and $\Delta\theta$ are too small. Thus, an adaptive adjustment, which has larger ΔI and $\Delta\theta$ values during large power change transient and smaller ones during steady state, is adopted to improve the overall performance. Also, the size of the hysteresis bound should be taken into account to improve the power quality.

Finally, a graphic comparison of computational burden between the scalar control and the proposed SRPC method is shown in Fig. 6. It should be mentioned that those methods were established based on the same MCU, dsPIC30F2020, with 30 million instructions per second to make a clear comparison [18]. Moreover, the sinusoidal function and the arctangent function in both Figs. 1 and 2 are not included for comparison

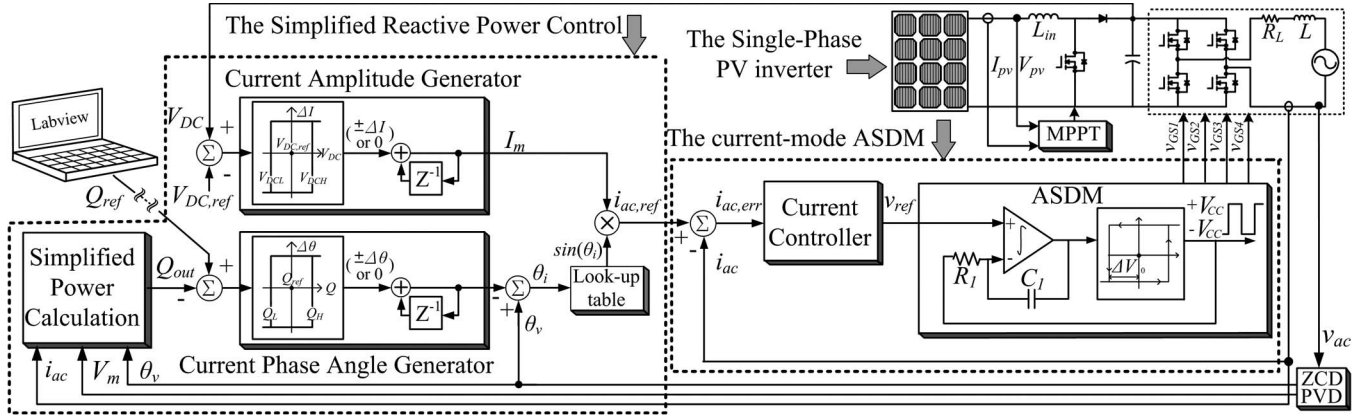


Fig. 7. Block diagram of the single-phase grid-connected PV inverter with the proposed control method.

because they can be implemented by a simple lookup table. Obviously, the reduction of the computational time of the proposed SRPC strategy is almost 23% of the one for the scalar control method.

III. CURRENT CONTROL STRATEGY

The block diagram of the single-phase PV inverter with the proposed control strategy is shown in Fig. 7. The power stage of the PV inverter consists of a boost converter with the maximum power point tracking (MPPT) function and a full-bridge inverter with both active and reactive power output. The control algorithm consists of the SRPC method and the CASDM control strategy.

The objective of the proposed PV inverter is to extract the maximum power from the PV panels and to inject the corresponding active power into the utility grid. In the meantime, the output reactive power Q_{out} calculated by the simplified power calculation and the reactive power command Q_{ref} sent by the user via the EIA-485 communication are compared to determine the phase shift of the current reference, θ_i . The amplitude and the phase angle of the grid voltage are captured by using the peak value detector (PVD) and the zero-crossing detector (ZCD), respectively. It should be mentioned that the ZCD along with the PVD is an easy-to-implement approach. On the other hand, the performance of the proposed SRPC method can be further improved by using a PLL circuit.

For the PV inverter's active power control, the voltage V_{DC} should be regulated by the current amplitude generator with a hysteresis comparator to generate the current reference's amplitude I_m . The algorithm of the current amplitude generator to regulate the voltage V_{DC} can be expressed as

$$\begin{aligned} &\text{if } V_{DC} > V_{DCH} \text{ then } k = +1; \\ &\text{else if } V_{DC} < V_{DCL} \text{ then } k = -1; \\ &\text{else } k = 0; \\ &I_m(n+1) = I_m(n) + k \times \Delta I. \end{aligned} \quad (9)$$

Eventually, the current reference $i_{ac,ref}$ is obtained by multiplying the current amplitude I_m with the signal $\sin(\theta_i)$. For

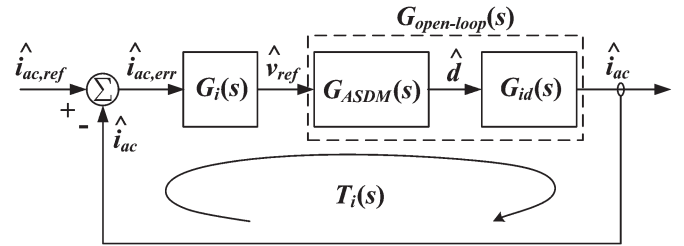


Fig. 8. Current control block diagram of the proposed PV inverter.

the output current control, the measured output current i_{ac} is compared with the current reference $i_{ac,ref}$ to generate the current error signal $i_{ac,err}$ which is sent into a current controller to generate the voltage reference v_{ref} . Then, the ASDM, which is an analog-to-digital signal converter with various frequency feature, is adopted to generate the gate signals, $v_{GS1}-v_{GS4}$. The single-phase grid-connected inverter with the ASDM was originally proposed by the authors in [15]. The authors design the CASDM control with a feedforward compensation to achieve the better performance. However, only steady-state analysis is discussed in that paper. It is important to improve the transient response by the small signal analysis, so the stability analysis is presented in the following.

The current control block diagram is redrawn in Fig. 8. The open-loop gain is represented as $G_{open-loop}(s)$, which consists of ASDM's transfer function $G_{ASDM}(s)$ and the control-to-output current transfer function $G_{id}(s)$. For steady-state analysis, the dc bus voltage V_{DC} and the grid voltage v_{ac} are assumed to be steady without disturbance. The compensated current loop gain $T_i(s)$ can be expressed as

$$T_i(s) = G_i(s)G_{ASDM}(s)G_{id}(s) \quad (10)$$

where $G_i(s)$ is the transfer function of the current controller.

In order to perform the stability analysis, the $G_{open-loop}(s)$ should be determined in advance. The $G_{id}(s)$ and $G_{ASDM}(s)$ can be derived by using a state space averaging method [19]–[21]. In the following, the transfer function of the open-loop gain $G_{open-loop}(s)$ and the compensated loop gain $T_i(s)$ will be derived.

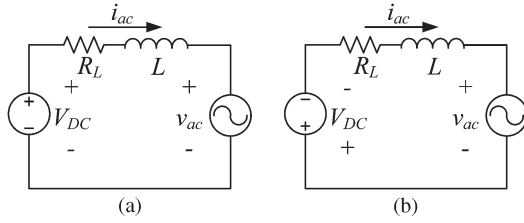


Fig. 9. Equivalent circuit diagram of the full-bridge inverter with bipolar voltage switching. (a) During dT time interval. (b) During $(1-d)T$ time interval.

A. $G_{id}(s)$

The full-bridge inverter is operated in bipolar voltage switching to prevent the leakage current flowing through the parasitic capacitance of the PV panels [22], [23]. Therefore, the voltage appearing at the left-hand side of the output inductor is either V_{DC} during the dT time interval or $-V_{DC}$ during the $(1-d)T$ time interval. The equivalent circuits of the full-bridge inverter during different time intervals are shown in Fig. 9(a) and (b) while the state equations are expressed as (11) and (12), respectively

$$\frac{di_{ac}}{dt} = \frac{(V_{DC} - R_L i_{ac} - v_{ac})}{L} \quad (11)$$

$$\frac{di_{ac}}{dt} = \frac{-(V_{DC} + R_L i_{ac} + v_{ac})}{L}. \quad (12)$$

By averaging the state equations with the duty cycle as the weighting factor, the following averaged state equation can be obtained:

$$\frac{di_{ac}}{dt} = \frac{(2d-1)V_{DC} - R_L i_{ac} - v_{ac}}{L}. \quad (13)$$

Since each of the output current i_{ac} and the duty cycle d consists of a dc component and an ac disturbance term, expressions of $i_{ac} = I_{ac} + \hat{i}_{ac}$ and $d = D + \hat{d}$ can be plugged into (13), and the small signal equation of the ac model can be obtained

$$\frac{d\hat{i}_{ac}}{dt} = \frac{2\hat{d}V_{DC} - R_L \hat{i}_{ac}}{L}. \quad (14)$$

By applying the Laplace transformation to (14), the control to output current transfer function in the frequency domain can be obtained

$$G_{id}(s) = \frac{\hat{i}_{ac}(s)}{\hat{d}(s)} = \frac{2V_{DC}}{sL + R_L}. \quad (15)$$

Equation (15) reveals that the $G_{id}(s)$ is a first-order system and its left-hand side pole is affected by the inductance L and the equivalent series resistance R_L of the output inductor. Because the full-bridge inverter is operated in a step-down mode, the voltage V_{DC} should be regulated to be higher than the peak value of the grid voltage. Moreover, the value of inductance L is determined according to the grid-connected standard which requires the total harmonic distortion (THD) of the injected current to be less than 5%.

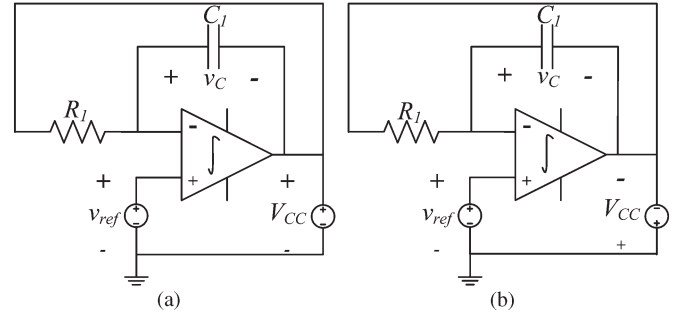


Fig. 10. Equivalent circuits of ASDM for different duty cycle intervals. (a) During dT time interval. (b) During $(1-d)T$ time interval.

B. $G_{ASDM}(s)$

The equivalent circuits of the ASDM function block diagram during duty cycle dT and $(1-d)T$ time intervals are shown in Fig. 10(a) and (b), respectively. The state equations can be written as

$$\frac{dv_C}{dt} = \frac{V_{CC} - v_{ref}}{R_1 C_1} \quad (16)$$

$$\frac{dv_C}{dt} = \frac{-(V_{CC} + v_{ref})}{R_1 C_1}. \quad (17)$$

The averaged state equations with the duty cycle as the weighting factor can be expressed as

$$\frac{dv_C}{dt} = \frac{(2d-1)V_{CC} - v_{ref}}{R_1 C_1}. \quad (18)$$

By introducing the ac disturbances, i.e., \hat{v}_{ref} , \hat{v}_c , and \hat{d} , into the variables in (18) and eliminating the dc terms, the small signal equation of the ASDM function block can be achieved

$$\frac{d\hat{v}_{ref}}{dt} = \frac{2\hat{d}V_{CC} - \hat{v}_{ref}}{R_1 C_1}. \quad (19)$$

In (19), it should be mentioned that the \hat{v}_c should be equal to the \hat{v}_{ref} since the virtual-short feature of the op-amps for the small signal model.

Similarly, by taking the Laplace transformation of (19), the mathematical expression of the ASDM in the frequency domain can be obtained

$$G_{ASDM}(s) = \frac{\hat{d}(s)}{\hat{v}_{ref}(s)} = \frac{sR_1 C_1 + 1}{2V_{CC}}. \quad (20)$$

Equation (20) reveals that the transfer function of the ASDM has a left-hand side zero, which is determined by the time constant $R_1 C_1$ of the integrator. Moreover, the switching frequency range of the ASDM, which is determined by the time constant $R_1 C_1$, the output voltage V_{CC} , and the hysteresis band of the comparator ΔV , can be expressed as

$$f_s = \frac{V_{CC}^2 - |V_{ref}|^2}{4R_1 C_1 \Delta V V_{CC}}. \quad (21)$$

In other words, the values of $R_1 C_1$, V_{CC} , and ΔV are selected to decide the switching frequency range.

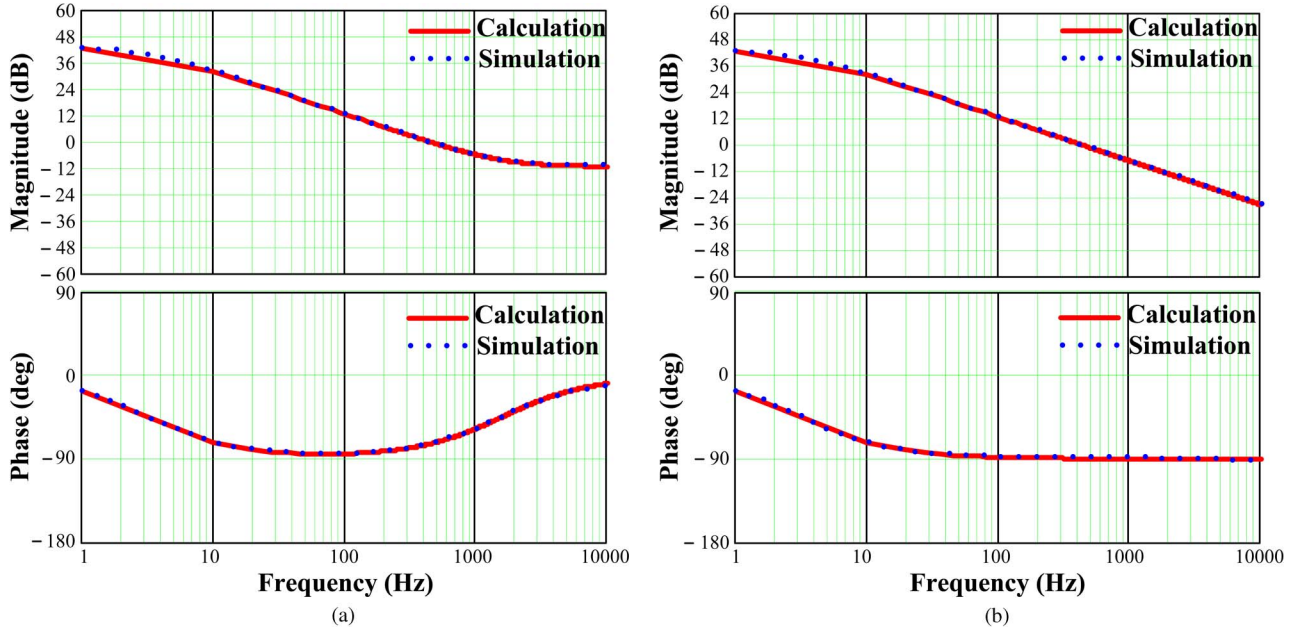


Fig. 11. Calculated and simulated Bode plots of the PV inverter with the CASDM. (a) Bode plots of $G_{open-loop}(s)$. (b) Bode plots of $T_i(s)$.

By combining (15) and (20), the open-loop gain of the PV inverter with the CASDM can be derived as

$$G_{open-loop}(s) = G_{ASDM}(s)G_{id}(s) = \frac{\hat{i}_{ac}(s)}{\hat{v}_{ref}(s)} = \frac{V_{DC}(sR_1C_1 + 1)}{V_{CC}(sL + R_L)}. \quad (22)$$

Typical circuit parameters are selected for the stability analysis illustration. They are $R_1 = 10 \text{ k}\Omega$, $C_1 = 10 \text{ nF}$, $R_L = 0.1 \Omega$, $L = 5 \text{ mH}$, $V_{DC} = 200 \text{ V}$, and $V_{CC} = 15 \text{ V}$. Bode plots of the $G_{open-loop}(s)$ are obtained by using both the mathematic computer software MathCAD and the circuit simulation tool Simplis.

Fig. 11(a) shows the calculated and simulated Bode plots of $G_{open-loop}(s)$ which is the open-loop gain of the PV inverter with the CASDM. It can be seen that the calculated Bode plot obtained by the derived equation and the simulated one obtained by the simulation software agree with each other. It verifies the validity of the derived equations. From (22), the zero and pole will cancel out after a certain frequency, and the magnitude of $G_{open-loop}(s)$ remains constant. Thus, the magnitude's attenuation at the switching frequency region is limited. It implies that the control loop can be easily affected by switching frequency ripple.

In order to guarantee the system's stability, the feedback loop with appropriate poles should be added in the control loop. Basically, a single-pole controller can provide a pole to cancel out the ASDM's zero. Therefore, the single-pole controller with a dc gain K has been adopted to implement the current controller which is determined as $G_i(s) = K/(sR_fC_f + 1)$. Eventually, the compensated current loop gain becomes

$$T_i(s) = G_i(s)G_{open-loop}(s) = \frac{KV_{DC}(sR_1C_1 + 1)}{V_{CC}(sL + R_L)(sR_fC_f + 1)}. \quad (23)$$

The calculated and simulated Bode plots for the $T_i(s)$ are shown in Fig. 11(b). The pole of $G_i(s)$ is selected to cancel the zero of $G_{ASDM}(s)$ to achieve the necessary gain margin and phase margin. By comparing Fig. 11(a) with (b), it can be seen that the magnitude of the $T_i(s)$ has a -20-dB/dec slope at high frequency and its phase margin is about 90° . The magnitude of the $T_i(s)$ at 10 kHz has been decayed significantly by comparing to the $G_{open-loop}(s)$. Both the calculated and simulated Bode plots show that the control loop of the CASDM can successfully eliminate the switching frequency ripple with a basic feedback controller. It should be mentioned that the stability and dynamic response can be further improved by adding a more sophisticated compensator in the feedback control loop.

More computer simulations are shown to verify the CASDM control strategy. According to (21), the predictive switching frequency range should be from 18.4 to 46.9 kHz with the parameters $V_{ref} = 11.7 \sin \omega t$, $R_1C_1 = 0.1 \text{ ms}$, $\Delta V = 0.8 \text{ V}$, and $V_{CC} = 15 \text{ V}$.

Fig. 12(a) shows the frequency spectrum of the PV inverter's output current with and without compensation. Fig. 12(b) shows the waveforms of the output current (top) corresponding to the reference signal (bottom). The partially expanded waveforms of Fig. 12(b) at minimum switching frequency $f_{s,min}$ region and maximum switching frequency $f_{s,max}$ region are shown in Fig. 12(c) and (d), respectively.

From Fig. 12(a), the switching frequency range of the PV inverter without compensation is shifted to a higher frequency region. It is because the reference signal contains the switching frequency ripple, as shown in Fig. 12(c) and (d). It should be mentioned that (21) is derived by assuming that the reference signal is almost constant within one switching period due to the fact that its frequency is much smaller than the switching frequency.

On the other hand, the high frequency ripple can be eliminated, as shown in Fig. 12(c) and (d), by using a proper current controller. Therefore, the switching frequency range of

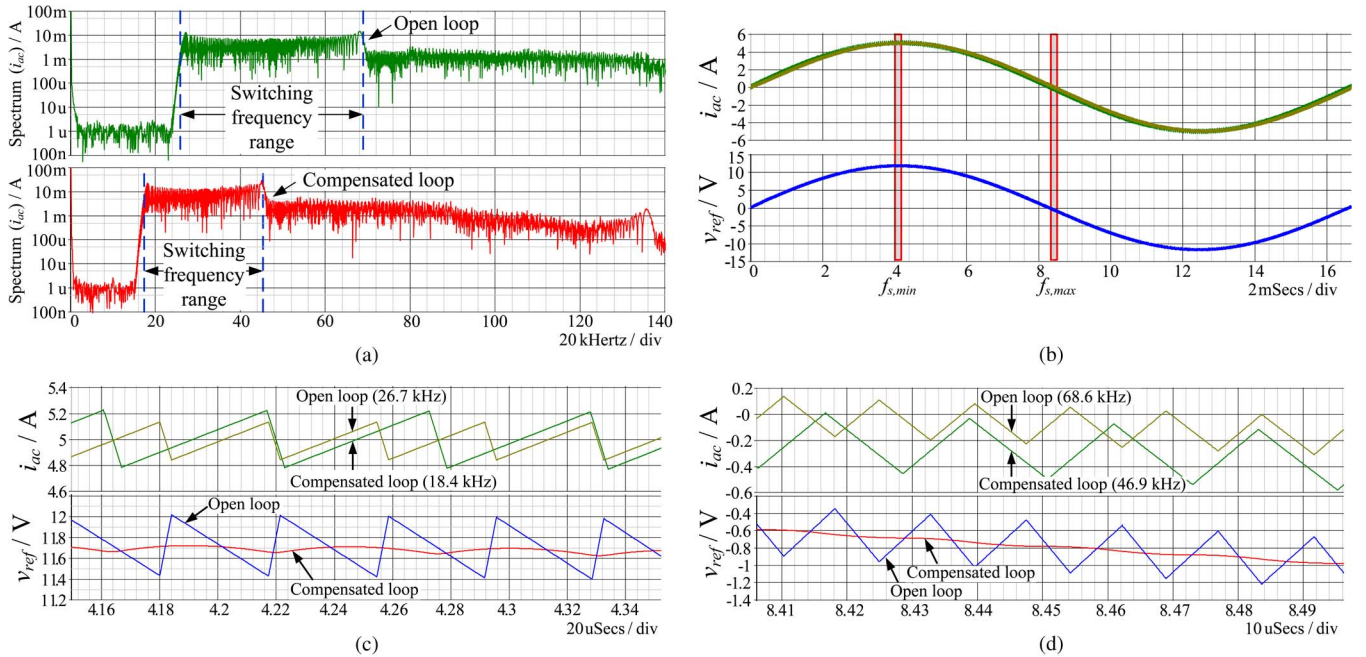


Fig. 12. Computer simulations for PV inverters with the CASDM control strategy. (a) Frequency spectrum of the PV inverter’s output current with and without compensation. (b) (top) Waveforms of output current corresponding to the (bottom) reference signal. (c) Partially expanded waveforms of Fig. 12(b) at minimum switching frequency $f_{s,min}$ region. (d) Partially expanded waveforms of Fig. 12(b) at maximum switching frequency $f_{s,max}$ region.

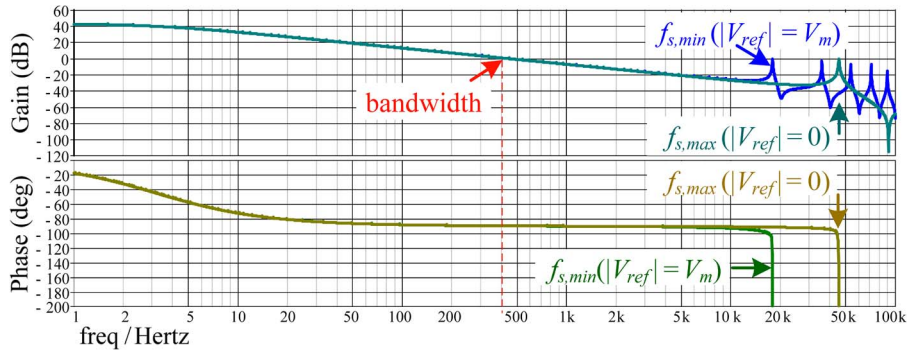


Fig. 13. Simulated Bode plots of $T_i(s)$ corresponding to different voltage reference signals V_{ref} .

the PV inverter with compensation can be predicted, as shown in Fig. 12(a), which agrees with (21).

For the PV inverter with the proposed CASDM, the voltage reference signal V_{ref} can be assumed to be a constant value during a switching period. Therefore, the CASDM can be assumed to have a “fixed” switching frequency during a short period of time. When the state space averaging method is applied to the CASDM, different plots can be obtained based on different switching frequencies. These plots have the same magnitude and phase angle feature for the low-frequency range as shown in Fig. 13. When the reference signal equals its peak value, $|V_{ref}| = V_m$, the CASDM has the minimum switching frequency, $f_{s,min} = 18.4$ kHz. On the contrary, the CASDM has the maximum switching frequency, $f_{s,max} = 46.9$ kHz, when the reference signal equals to zero, $|V_{ref}| = 0$. Within the half of the $f_{s,min}$, the magnitude and phase angle are identical. In order to ensure the model’s accuracy, the system bandwidth should be designed within the half of the $f_{s,min}$. On the other hand, the low-frequency analysis is sufficient for the

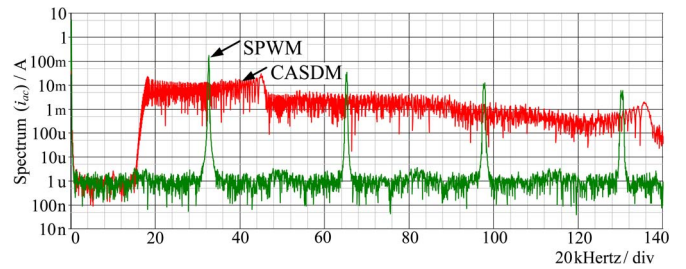


Fig. 14. Current harmonic spectrum of the PV inverter with different control methods.

grid-tied PV inverter with very slow power changes. Therefore, the derived model is reliable for the grid-tied PV inverter with CASDM control.

The current harmonic spectrum of the PV inverter with different current control strategies is shown in Fig. 14.

It should be mentioned that the average switching frequency of the proposed CASDM is equal to the one for SPWM and

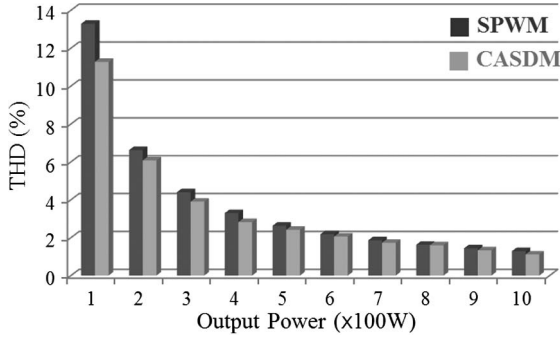


Fig. 15. Calculated THD of the output current with different control methods.

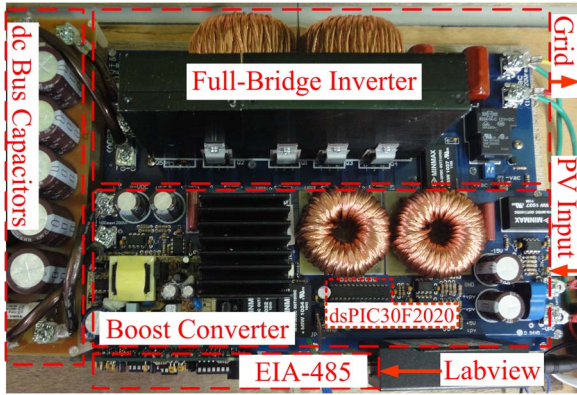


Fig. 16. Photograph of the prototype PV inverter.

both of the inverters are operated in the bipolar voltage switching. It can be seen that the CASDM has various switching frequencies which can spread switching noise over a wider frequency spectrum. It has the merit of low electromagnetic interference.

The calculated THD for the PV inverter with different current control strategies is shown in Fig. 15. The PV inverter with the CASDM can reduce the harmonic current compared to that with the conventional SPWM method.

IV. EXPERIMENTAL RESULTS

Fig. 16 shows the photograph of the prototype PV inverter which consists of the boost converter and the full-bridge inverter. Moreover, the human-machine interface, Labview, with the EIA-485 communication is integrated into the PV inverter to deliver the reactive power command. All of the control algorithms are implemented by using the low-cost 16-b MCU, dsPIC30F2020. The specifications of the prototype PV inverter are listed in Table I.

It should be mentioned that the PV simulator, Agilent E4360A, is used to replace the actual PV arrays and the power analyzer, YOKOGAWA WT-1800, is connected to the PV inverter to measure the active output power and the reactive output power.

To verify the performance of the proposed PV inverter with the SRPC, two tests are performed. Test 1 shows that the change of reactive power will not affect the PV inverter’s MPPT function, while Test 2 verifies that the reactive power output

TABLE I
SPECIFICATIONS OF PROTOTYPE PV INVERTER

Parameter	Symbol	Value
Input voltage range	V_{pv}	0 - 120 V
Input current range	I_{pv}	0 - 10 A
Input inductance / ESR	L_{in} / R_{in}	1mH / 0.3Ω
Boost converter's switching frequency	f_{s1}	20 kHz
dc bus voltage / capacitor	V_{DC} / C_{DC}	200V / 2350μF
Grid voltage / frequency	v_{ac} / f_{ac}	110V _{rms} / 60Hz
Output inductance / ESR	L / R_L	4mH / 1.2Ω
Full-bridge inverter's switching frequency	f_{s2}	18.4 - 46.9 kHz

will not be affected by the abrupt input PV power change. Details of the experimental measurements are shown as follows.

Test 1: Key measured waveforms of the proposed PV inverter with constant active power but various reactive powers are shown in Fig. 17. The edge-triggered sampling signals S_1 and S_2 , which are successfully generated by using the analog ZCD, along with the ac line voltage waveform are shown in Fig. 17(a). Then, the active current component i_p and the reactive current component i_q can be obtained by sampling the ac current value at times t_p and t_q , respectively.

Fig. 17(b) shows key waveforms of the dc bus voltage V_{DC} , ac line voltage v_{ac} , and ac line current i_{ac} . In the beginning, the active output power is around 680 W, and the reactive power command is set to 0 var. At time t_1 , the reactive power command is abruptly changed from 0 to 600 var. Thus, the amplitude and the phase angle of current i_{ac} rise due to the increment of reactive power command.

Both the measured active power P and reactive power Q during the entire time period are shown in Fig. 17(c). It can be found that the proposed SRPC and the CASDM method can smoothly control the PV inverter’s reactive output power without causing seriously active power drop.

Fig. 17(d) shows the transient behavior of the ac current increment during time interval t_1-t_2 of Fig. 17(b). Both the amplitude and phase angle of the ac current increase gradually. Also, it can be seen that the ac current is almost sinusoidal during the transition. It implies that the current distortion is very low.

The partially expanded waveforms of Fig. 17(b) before time t_1 are shown in Fig. 17(e). Obviously, the ac line voltage and the current are almost in phase because of the zero reactive power setting. In addition, the measured currents i_p and i_q are 8.75 and 0 A, respectively. Based on (5.a) and (6.a), the active power and reactive power are calculated as 683 W and 0 var, which agree with Fig. 17(c).

The partially expanded waveform of Fig. 17(b) after time t_2 is shown in Fig. 17(f) where the measured currents i_p and i_q are 8.5 and 7.75 A, respectively. Therefore, the active power and reactive power are calculated as 663 W and 605 var, which agree with Fig. 17(c).

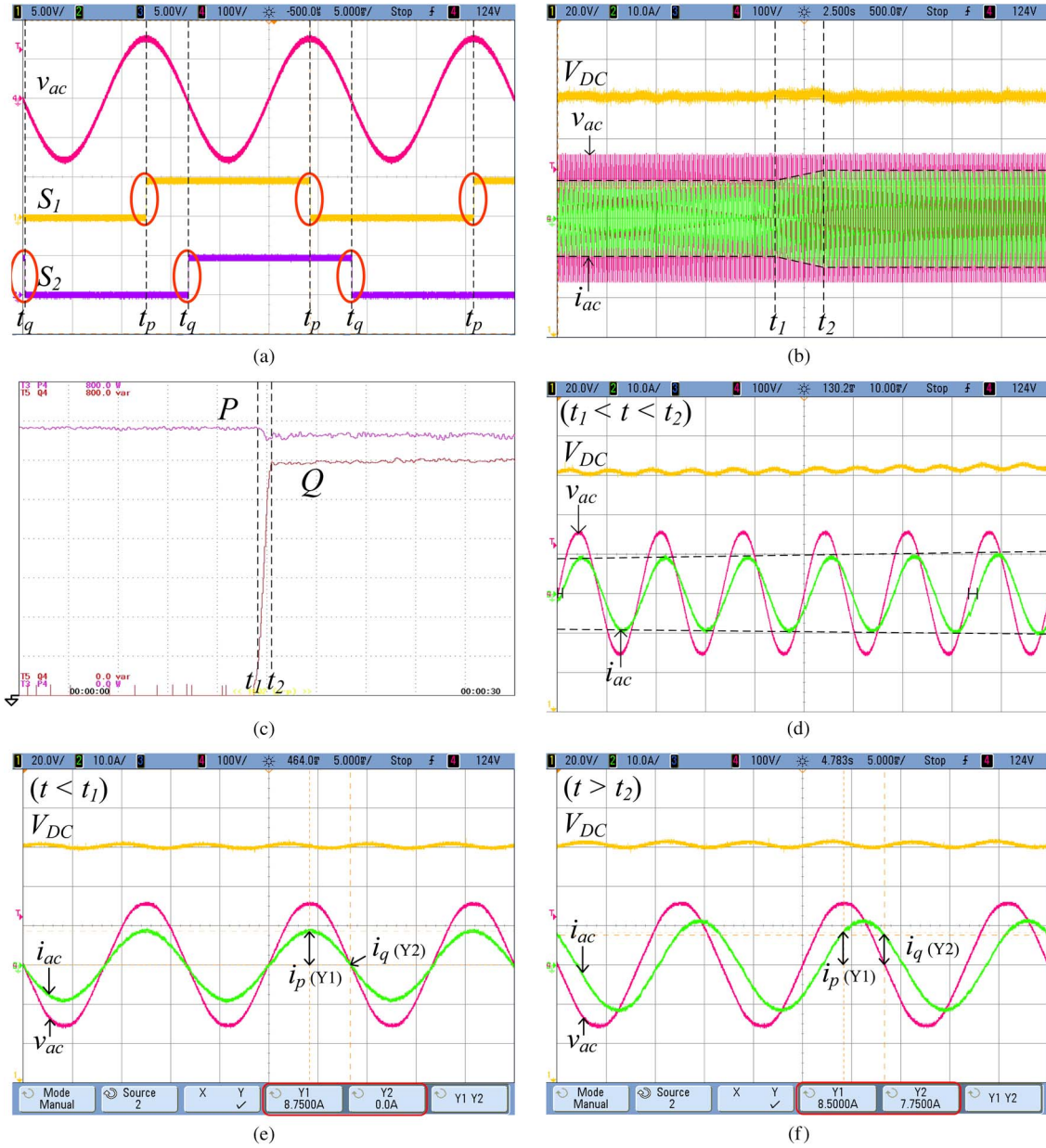


Fig. 17. Key measured waveforms of the proposed PV inverter with constant active power but various reactive powers. (a) (S_1 : 5 V/div; S_2 : 5 V/div; v_{ac} : 100 V/div; t : 5 ms/div). (b) (V_{DC} : 20 V/div; v_{ac} : 100 V/div; i_{ac} : 10 A/div; t : 500 ms/div). (c) (P_{AC} : 100 W/div; Q_{AC} : 100 var/div; t : 3 s/div). (d) (V_{DC} : 20 V/div; v_{ac} : 100 V/div; i_{ac} : 10 A/div; t : 10 ms/div). (e) (V_{DC} : 20 V/div; v_{ac} : 100 V/div; i_{ac} : 10A/div; t : 5 ms/div). (f) (V_{DC} : 20 V/div; v_{ac} : 100 V/div; i_{ac} : 10 A/div; t : 5 ms/div).

In Fig. 17, it can be found that the active power remains almost unchanged while the measured reactive power has been greatly changed from 0 to 605 var. In other words, the PV inverter with the SRPC and the CASDM can achieve the desired RPC without affecting the MPPT operation.

Test 2: Key measured waveforms of the proposed PV inverter under different active power but constant reactive power operation are shown in Fig. 18.

Fig. 18(a) shows the PV simulator’s voltage V_{pv} , current I_{pv} , and power P_{pv} . In the beginning, the maximum output power of the PV simulator is set to 750 W, and the reactive power command is set to 300 var. At time t_3 , the maximum output power of the PV simulator is changed from 750 to 550 W abruptly. During the transient time interval, $t_3 \sim t_4$, the PV

inverter gradually decreases its extracting power from the PV simulator with the MPPT feature. After time t_4 , the extracted power by the PV inverter reaches the stable maximum value.

The dc bus voltage V_{DC} , ac line voltage v_{ac} , and ac line current i_{ac} are shown in Fig. 18(b). Due to the decrement of the PV simulator’s output power, the injected sinusoidal current decreases smoothly during the time interval, t_3-t_4 .

Both the measured active power P and reactive power Q during the entire time period are shown in Fig. 18(c). It can be found that the PV inverter can maintain constant reactive power output despite the abruptly active power drop.

Fig. 18(d) shows the transient behavior of the ac current decrement during time interval t_3-t_4 . It can be seen that both the amplitude and phase angle of the injected current decrease

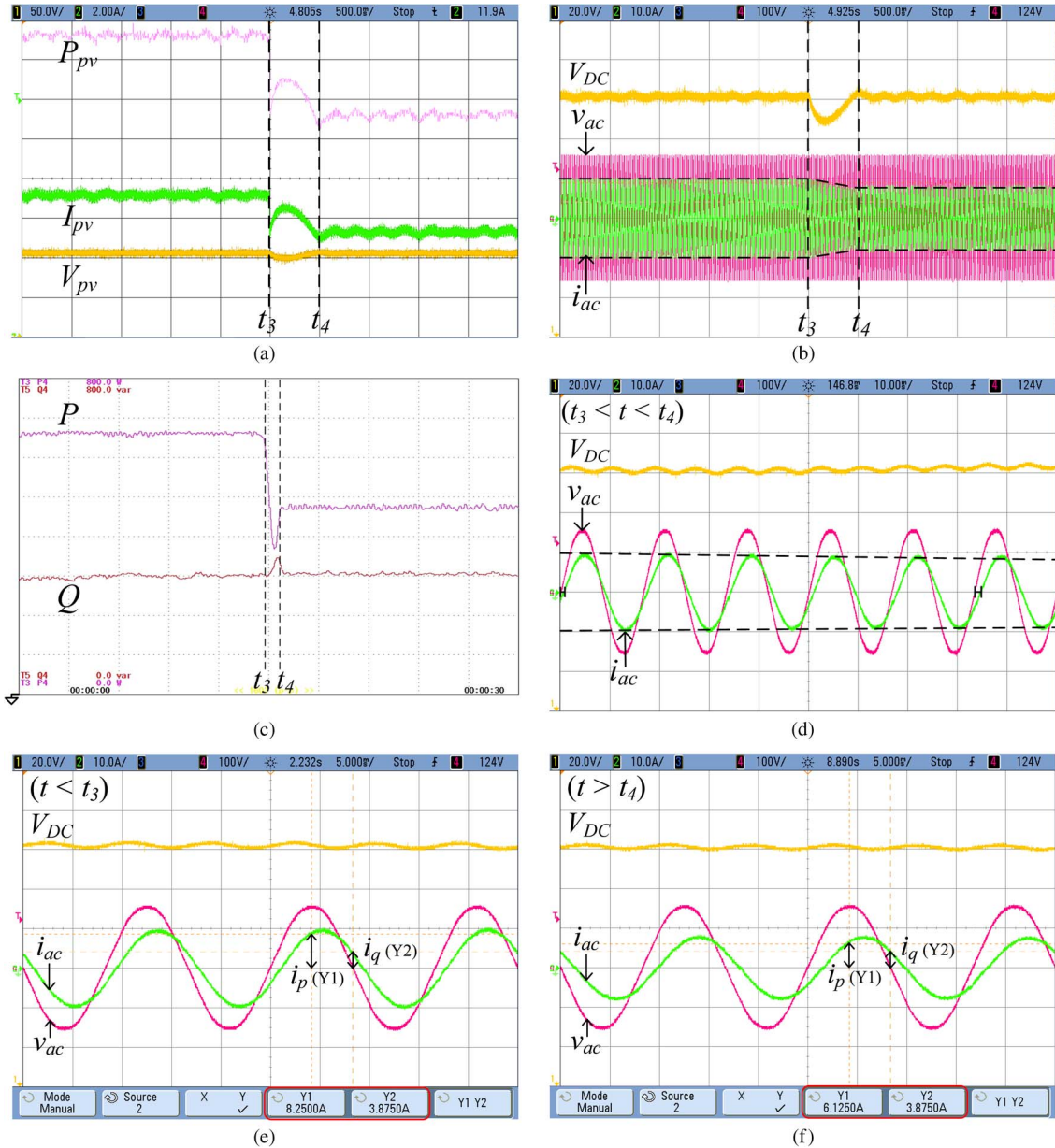


Fig. 18. Key measured waveforms of the proposed PV inverter with the constant reactive power but various active powers. (a) (P_{pv} : 100 W/div; I_{pv} : 2 A/div; V_{pv} : 50 V/div; t : 500 ms/div). (b) (V_{DC} : 20 V/div; v_{ac} : 100 V/div; i_{ac} : 10 A/div; t : 500 ms/div). (c) (P_{AC} : 100 W/div; Q_{AC} : 100 var/div; t : 3 s/div). (d) (V_{DC} : 20 V/div; v_{ac} : 100 V/div; i_{ac} : 10 A/div; t : 10 ms/div). (e) (V_{DC} : 20 V/div; v_{ac} : 100 V/div; i_{ac} : 10 A/div; t : 5 ms/div). (f) (V_{DC} : 20 V/div; v_{ac} : 100 V/div; i_{ac} : 10 A/div; t : 5 ms/div).

gradually. It verifies that the proposed SRPC and the CASDM can achieve very good active and reactive power transient control.

The partially expanded waveforms of Fig. 18(b) before time t_3 are shown in Fig. 18(e). The measured currents i_p and i_q are 8.25 and 3.875 A, respectively. Therefore, the active power and reactive power are calculated as 644 W and 302 var. Similarly, the partially expanded waveform of Fig. 18(b) after time t_4 is shown in Fig. 18(f) where the measured currents i_p and i_q are 6.125 and 3.875 A, respectively. Hence, the active power and reactive power are calculated as 478 W and 302 var.

From the measured waveforms shown in Fig. 18, it can be seen that the measured active power changes from 644 to 478 W while the measured reactive power remains unchanged. It re-

veals that the PV inverter with the proposed SRPC and the CASDM can achieve the constant RPC without being affected by the abrupt active power drop.

V. CONCLUSION

This paper proposed a SRPC method along with the CASDM for the single-phase grid-connected PV inverter with RPC. The proposed SRPC method can reduce the computational burden of the processor significantly, so a low-cost MCU can be adopted to implement the cost-effective PV inverter. Also, the small signal analysis for the CASDM is presented to prove the control stability. With both the SRPC and CASDM, the single-phase PV inverter can achieve the desired RPC with

low current harmonic distortion. Different experimental waveforms are presented to verify the performance of the prototype circuit.

REFERENCES

- [1] H. Kanchev, D. Lu, F. Colas, V. Lazarov, and B. Francois, "Energy management and operational planning of a microgrid with a PV-based active generator for smart grid applications," *IEEE Trans. Ind. Electron.*, vol. 58, no. 10, pp. 4583–4592, Oct. 2011.
- [2] C. Liu, P. Sun, J.-S. Lai, Y. Ji, M. Wang, C.-L. Chen, and G. Cai, "Cascade dual-boost/buck active-front-end converter for intelligent universal transformer," *IEEE Trans. Ind. Electron.*, vol. 59, no. 12, pp. 4671–4680, Dec. 2012.
- [3] H. J. Avelar, W. A. Parreira, J. B. Vieira, L. C. G. de Freitas, and E. A. A. Coelho, "A state equation model of a single-phase grid-connected inverter using a droop control scheme with extra phase shift control action," *IEEE Trans. Ind. Electron.*, vol. 59, no. 3, pp. 1527–1537, Mar. 2012.
- [4] X. Li and A. K. S. Bhat, "A utility-interfaced phase-modulated high-frequency isolated dual LCL dc/ac converter," *IEEE Trans. Ind. Electron.*, vol. 59, no. 2, pp. 1008–1019, Feb. 2012.
- [5] A. Cagnano, E. De Tuglie, M. Liserre, and R. A. Mastromauro, "Online optimal reactive power control strategy of PV inverters," *IEEE Trans. Ind. Electron.*, vol. 58, no. 10, pp. 4549–4558, Oct. 2011.
- [6] W. Sinsukthavorn, E. Ortjohann, A. Mohd, N. Hamsic, and D. Morton, "Control strategy for three-/four-wire-inverter-based distributed generation," *IEEE Trans. Ind. Electron.*, vol. 59, no. 10, pp. 3890–3899, Oct. 2012.
- [7] J. Liu, J. Yang, and Z. Wang, "A new approach for single-phase harmonic current detecting and its application in a hybrid active power filter," in *Proc. IEEE IECON/IECON*, 1999, pp. 849–854.
- [8] M. Saitou, N. Matsui, and T. Shimizu, "A control strategy of single-phase active filter using a novel d-q transformation," in *Conf. Rec. IEEE 38th IAS Annu. Meeting*, 2003, pp. 1222–1227.
- [9] M. Saitou and T. Shimizu, "Generalized theory of instantaneous active and reactive powers in single-phase circuits based on Hilbert transform," in *Proc. IEEE PESC*, 2002, pp. 1419–1424.
- [10] Q. Zhang, X.-D. Sun, Y.-R. Zhong, M. Matsui, and B.-Y. Ren, "Analysis and design of a digital phase-locked loop for single-phase grid-connected power conversion systems," *IEEE Trans. Ind. Electron.*, vol. 58, no. 8, pp. 3581–3592, Aug. 2011.
- [11] S. Xu, J. Wang, and J. Xu, "A current decoupling parallel control strategy of single-phase inverter with voltage and current dual closed-loop feedback," *IEEE Trans. Ind. Electron.*, vol. 60, no. 4, pp. 1306–1313, Apr. 2013.
- [12] R. I. Bojoi, L. R. Limongi, D. Roiu, and A. Tenconi, "Enhanced power quality control strategy for single-phase inverters in distributed generation systems," *IEEE Trans. Power Electron.*, vol. 26, no. 3, pp. 798–806, Mar. 2011.
- [13] L. Liu, H. Li, Z. Wu, and Y. Zhou, "A cascaded photovoltaic system integrating segmented energy storages with self-regulating power allocation control and wide range reactive power compensation," *IEEE Trans. Power Electron.*, vol. 26, no. 12, pp. 3545–3559, Dec. 2011.
- [14] P. Sun, C. Liu, J.-S. Lai, and C.-L. Chen, "Grid-tie control of cascade dual-buck inverter with wide-range power flow capability for renewable energy applications," *IEEE Trans. Power Electron.*, vol. 27, no. 4, pp. 1839–1849, Apr. 2012.
- [15] Y.-M. Chen, C.-H. Chang, and K.-Y. Liu, "Grid-tied inverter with current-mode asynchronous sigma-delta modulation," in *Proc. IEEE ECCE*, 2009, pp. 928–933.
- [16] C.-H. Chang, F.-Y. Wu, and Y.-M. Chen, "Modularized bidirectional grid-connected inverter with constant-frequency asynchronous sigma-delta modulation," *IEEE Trans. Ind. Electron.*, vol. 59, no. 11, pp. 4088–4100, Nov. 2012.
- [17] J. Paramesh and A. von Jouanne, "Use of sigma-delta modulation to control EMI from switch-mode power supplies," *IEEE Trans. Ind. Electron.*, vol. 48, no. 1, pp. 111–117, Feb. 2001.
- [18] *Dspic30f Math Library*, Microchip Technology Inc., Chandler, AZ, USA, 2004.
- [19] C.-L. Chen, Y. Wang, J.-S. Lai, Y.-S. Lee, and D. Martin, "Design of parallel inverters for smooth mode transfer microgrid applications," *IEEE Trans. Power Electron.*, vol. 25, no. 1, pp. 6–15, Jan. 2010.
- [20] N. Mohan, T. M. Undeland, and W. P. Robbins, *Power Electronics: Converters, Applications, and Design*, 3rd ed. Hoboken, NJ, USA: Wiley, 2003.
- [21] R. D. Middlebrook and S. Cuk, "A general unified approach to modeling switching-converter power stage," in *Proc. IEEE PESC*, 1976, pp. 18–34.
- [22] T. Kerekes, R. Teodorescu, P. Rodriguez, G. Vazquez, and E. Aldabas, "A new high-efficiency single-phase transformerless PV inverter topology," *IEEE Trans. Ind. Electron.*, vol. 58, no. 1, pp. 184–191, Jan. 2011.
- [23] S. V. Arahjo, P. Zacharias, and R. Mallwitz, "Highly efficient single-phase transformerless inverters for grid-connected photovoltaic system," *IEEE Trans. Ind. Electron.*, vol. 57, no. 9, pp. 3118–3128, Sep. 2010.



Chia-Hsi Chang (S'09) received the B.S. degree in electrical engineering from the National Taiwan University of Science and Technology, Taipei, Taiwan, in 2008. Since 2009, he has been working toward the Ph.D. degree in the Department of Electrical Engineering, National Taiwan University, Taipei.

In 2013, he joined the Future Energy Electronics Center, Virginia Polytechnic and State University, Blacksburg, VA, USA, as a Visiting Scholar, supported by the National Science Council, Taiwan. His research interests include the analysis, design, and control of grid-connected inverters, particularly for microgrid applications.



Yu-Hui Lin received the B.S. degree in electrical engineering from National Cheng Kung University, Tainan, Taiwan, in 2009 and the M.S. degree in electrical engineering from National Taiwan University, Taipei, Taiwan, in 2011.

In 2012, he joined the ASUSTek Computer International, Taipei, as a Power Engineer. His research interests include energy switching-mode power supply and renewable energy system.



Yaow-Ming Chen (S'96–M'98–SM'05) received the B.S. degree in electrical engineering from National Cheng Kung University, Tainan, Taiwan, in 1989 and the M.S. and Ph.D. degrees in electrical engineering from the University of Missouri, Columbia, MO, USA, in 1993 and 1997, respectively.

From 1997 to 2000, he was with I-Shou University, Kaohsiung, Taiwan, as an Assistant Professor. From 2000 to 2008, he was with National Chung Cheng University, Taiwan. In 2008, he joined National Taiwan University, Taipei, Taiwan, where he is currently a Professor in the Department of Electrical Engineering. His research interests include power electronic converters and renewable energy.



Yung-Ruei Chang (M'01) received the Ph.D. degree in electrical engineering from National Taiwan University, Taipei, Taiwan, in 2004.

He is currently the Director of the Smart Grid Laboratory of the Nuclear Instrumentation Division of the Institute of Nuclear Energy Research (INER), Atomic Energy Council, Taipei, where he has been working since 1994. From 2000 to 2004, he was involved in digital control, system reliability, and fault-tolerant system design related to nuclear power plant safety project. He spent one year as a Visiting Engineer at STN ATLAS, Bremen, Germany, and GE, Fairfield, CT, USA, in 2000. Since 2005, he has been responsible for power conditioning systems of the renewable energy project and led the distributed generation research group of INER. In 2007, he was a Visiting Scholar at the Future Energy Electronics Center of Virginia Polytechnic and State University, Blacksburg, VA, USA, where he joined to develop a high-efficiency dc-dc converter for solid oxide fuel cell. He is currently in charge of the microgrid project of INER. His research interests include system reliability analysis, fault-tolerant system, dependable computing, power electronic system, and microgrid technology.